2
Review of literature & Experimental Techniques

Solar photovoltaic has attracted considerable attention in both academia and industry because of its widespread application. Solar energy is an ultimate source of energy that can fulfill all our energy needs. Photovoltaic devices capture solar radiations and convert it into electricity for further use. Cu_2ZnSnS_4 (CZTS) is a potential material for photovoltaic energy conversion, considered in the present study and will be discussed later in more detail. The following sections will review about the photovoltaics in general including device parameters, equivalent circuit model and about CZTS materials.

2.1 Photovoltaics

Photovoltaic is a basic physical process that converts incident light energy (photons) into electricity (voltage). The history of photovoltaics goes back to 1839 when Alexandre Edmund Becquerel first observes the photovoltaic phenomena in a liquid electrolyte. However, it took a long time and the discovery of the first photovoltaic device was successful about 1954 in Bell laboratory, USA. The solar cell is essentially a p-n junction device and when the light of sufficient energy equivalent to the bandgap of the semiconductor forming the junction falls; electron-hole pairs will be generated. The energy of photon greater than the bandgap of semiconductor (hv-Eg) is lost in heating the material while photon with energy less than the bandgap will be completely lost and do not participate in the electron-hole generation and thus, the current conduction. The generated electron-hole pair is separated out by the electric field present at the space charge region of a p-n junction and finally collected at the outer circuit. Schematic representation of a solar cell and the band structure diagram at the p-n junction are shown in **Figure 2.1 (a, b).** When light shines on the device, Fermi levels get splatted and the difference in the Fermi level of n and p sides results into the open circuit voltage of the solar cell.

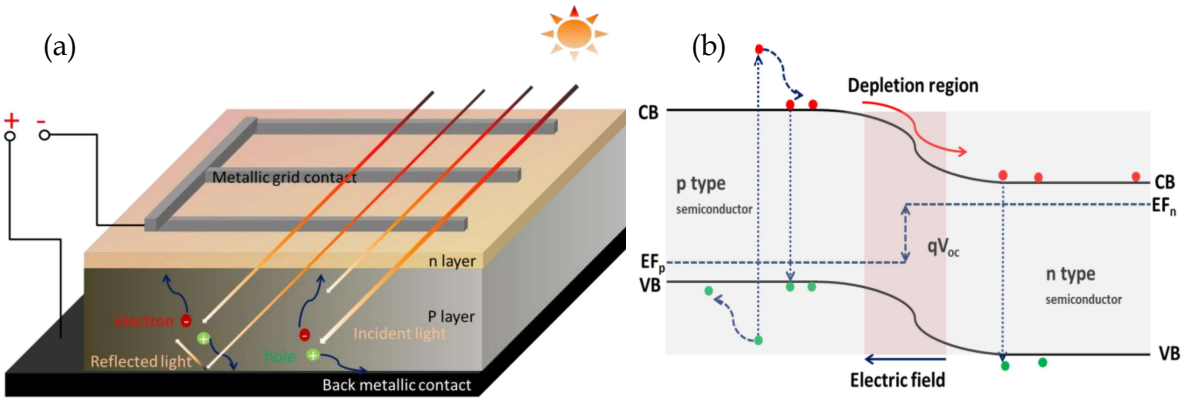

Figure 2.1 Schematic representation of (a) p-n junction solar cell (b) Band diagram of p-n junction under illumination.

2.2 Solar radiation

The solar spectrum is distributed over a range of energy and is nearly similar to a radiation coming out from a black body at temperature 6000 K. In atmosphere solar radiation gets attenuated by absorption and scattering due to different gases, water vapor and aerosol particles and the final solar radiation that reaches the earth surface depend on the path length that the light traverses through the atmosphere. Air mass (AM) gives a relative measure of how much a light traverses through the atmosphere and is defined as the ratio of path length that a light traverses through the atmosphere to the shortest possible path length given by $AM = \frac{1}{\cos\theta}$ where θ is the zenith angle. As can be seen in **Figure 2.2 (a)** when the sun is exactly overhead it is called AM 1. When light travels 50% more distance than the light from the sun when it is exactly overhead is called AM 1.5. At the earth surface, standard solar spectrum considered is AM 1.5G (where G stands for global) which includes both direct and diffuse spectra and has value 1000 W/m². AM 1.5D (where D stands for direct) includes only direct solar spectrum that reaches the earth surface and has value 963.56 W/m²[Liley, 2013]. **Figure 2.2 (b)** shows ASTM standard solar spectrum at different air mass.

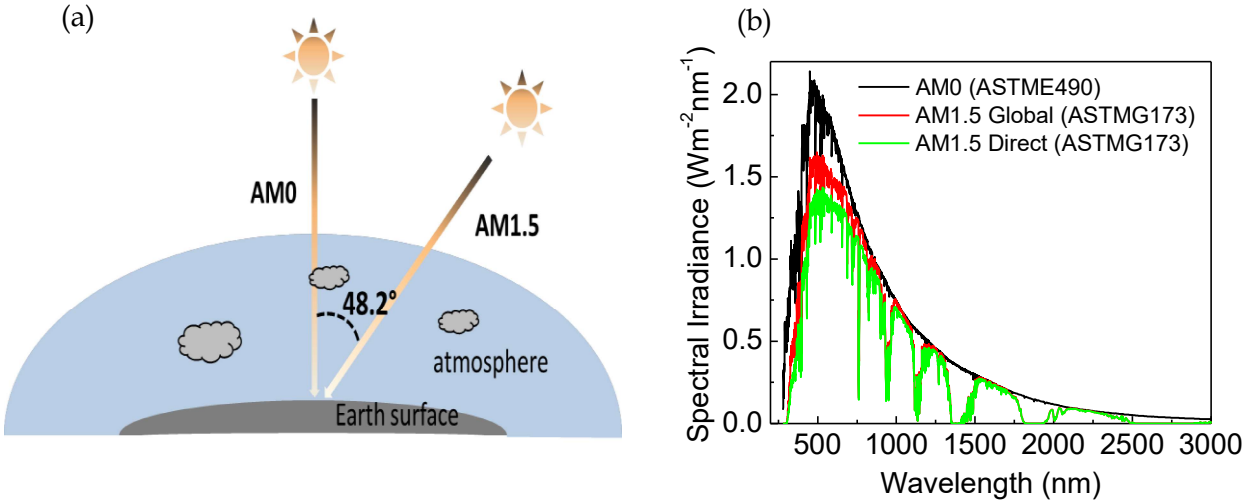

Figure 2.2 (a) schematic representation for air mass ratio (AM) definition (b) Solar irradiance versus wavelength curve for AM0, AM1.5G and AM1.5D solar spectra

2.3 Shockley Queisser Efficiency Limit

William Shockley and Hans Queisser in 1961 provided a detailed balanced limit for the maximum theoretical efficiency that a single p-n junction solar cell can produce, **Figure 2.3** [Shockley & Queisser, 1961]. The maximum light to solar power conversion under solar AM 1.5 G solar radiations is 33.16% corresponding to a semiconductor bandgap of 1.34 eV (928 nm) as shown in **Figure 2.3**

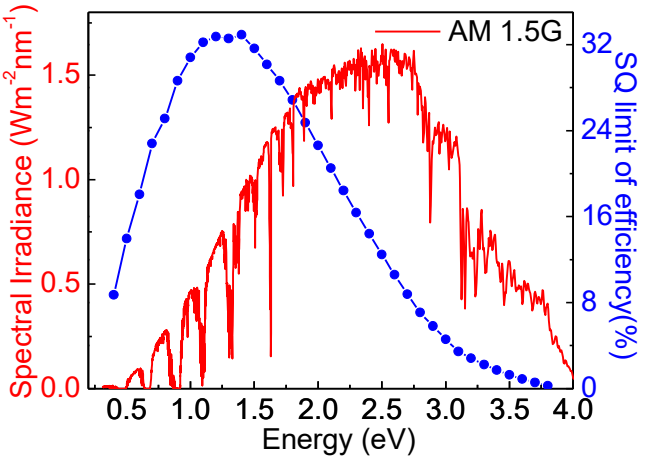

Figure 2.3 Solar AM1.5G spectrum and SQ limit of maximum efficiency of the single junction solar cell with respect to energy [Rühle, 2016]

2.4 Diode equivalent circuit and Current-voltage characteristics of the solar cell

The solar cell can be modeled as a single diode equivalent circuit which considers a current source in parallel with a diode. A single diode equivalent circuit for a practical solar cell also considers parasitic resistances due to contact resistance, quantified as series resistance Rs, and leakage current, quantified as shunt resistance Rsh, is shown in **Figure 2.4**[Sze & Ng, 2007].

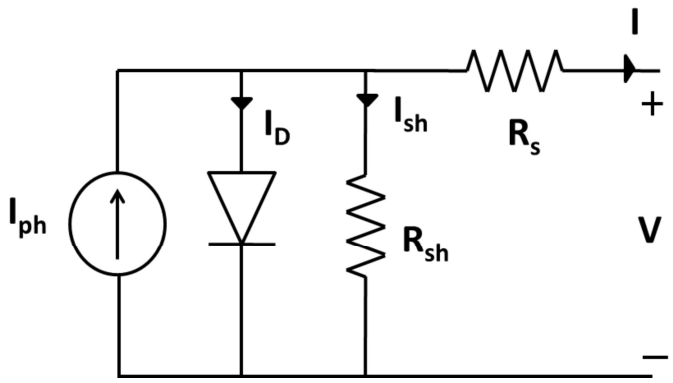

Figure 2.4 One diode equivalent circuits for a solar cell in conjunction with series and shunt resistances.

Current-voltage (I-V) characteristics for a solar cell consider loss due to contact resistance and leakage current through the device. These two effects add two parasitic resistances Rs and Rsh to the I-V characteristics of a solar cell which can be written as

$$I = I_{ph} - I_0\left(e^{\frac{V+IR_s}{nV_T}} - 1\right) - \frac{V + IR_s}{R_{sh}}$$

Where I_{ph} is the photocurrent, I_0 is reverse saturation current, n is ideality factor of the diode, V_T is thermal voltage. Single diode equivalent circuit of the solar cell does not consider loss due to recombination. In order to account recombination losses, an additional diode is inserted into the single diode equivalent circuit and is called two diode equivalent models for a solar cell which is shown in **Figure 2.5**

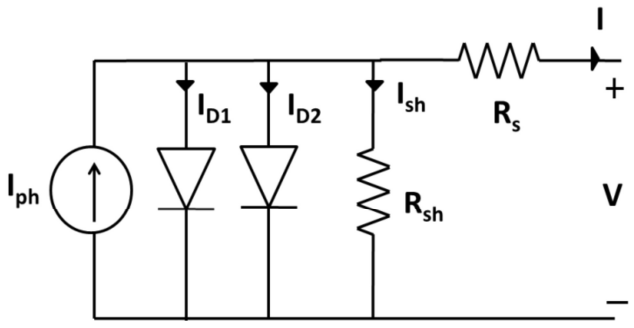

Figure 2.5 Two diode equivalent circuit for a solar cell

The current-voltage characteristics for two diode equivalent circuit of the solar cell is given by

$$I = I_{ph} - I_{01}\left(e^{\frac{V+IR_s}{n1V_T}} - 1\right) - I_{02}\left(e^{\frac{V+IR_s}{n2V_T}} - 1\right) - \frac{V + IR_s}{R_{sh}}$$

Where (I_{01}, n1) and (I_{02}, n2) is the reverse saturation current and diode ideality factor corresponding to diode D1 and D2, respectively [Schroder, 2005].
The power conversion efficiency of the solar cell can be written as

$$\eta = \frac{P_{max}}{P_{in}} x\ 100\ \%$$

Where $P_{max} = V_m I_m$ and P_{in} is power of incident light on the solar cell.

Fill factor of the solar cell is essentially a measure of the quality of solar cell and is defined as the ratio of the maximum power generated by a solar cell to the maximum theoretical power when both open circuit voltage (Voc) and short-circuit current (Isc) occur at the same time.

$$FF = \frac{V_m I_m}{V_{oc} I_{sc}}$$

The efficiency of the solar cell can also be rewritten as $\eta = \frac{V_{oc} I_{sc} FF}{P_{in}} x\ 100\ \%$. Parasitic resistances (Rs and Rsh) reduce the fill factor of the cell by dissipating power in the resistance hence ideally solar cell should have zero series resistance and infinite shunt resistance. Low shunt resistance of the solar cell can provide an alternate path to the photogenerated current and cause losses in current collected at the outer circuit. These parasitic resistances reduce the efficiency and FF of the solar cell.

2.5 Deposition of CZTS thin film

Quaternary compound semiconductor Cu_2ZnSnS_4 (CZTS) is one of the most provocative absorber layer materials in the thin film solar cell (TFSC). Variety of deposition techniques both vacuum and non-vacuum have been adopted for its synthesis. Material properties to a great extent depend on the deposition techniques. The present section gives a critical review of the widely adopted deposition techniques for CZTS and their impact on solar cell performance.

2.5.1 Sputtering

Sputtering is one of the most common vacuum-based deposition techniques for CZTSSe. In sputtering a solid target material is etched using DC/RF power source which gets deposited on the substrate. Two-step depositions are usually followed in sputter deposition. Metallic layers are either deposited in stacks sequentially or simultaneously on the substrate followed by high temperature thermal treatment in sulfur or selenium environment to form CZTSSe. In 1988 Ito and Nakazawa first showed the single step deposition of CZTS using CZTS compound target prepared by solid state reaction of stoichiometric composition of elements in a quartz ampoule at an elevated temperature of 1050 °C for 48 hour. Stannite phase of CZTS has been claimed to form showing a heterojunction open circuit voltage of 165 meV with cadmium tin oxide (CTO) [Ito & Nakazawa, 1988]. Tanaka et al. has showed CZTS deposition by annealing of sequentially deposited metallic Cu/Zn/Sn films using hybrid sputtering in sulfur flux for 60 min [T. Tanaka et al., 2005]. Jimbo et al. tried inline annealing system coupled with the sputtering chamber to restrict exposure to the environment. This way they have achieved an efficiency of 5.74% [Jimbo et al., 2007]. In 2008 Katagiri et al. from the same group for the first time has fabricated CZTS solar cell with efficiency exceeding 6.7% by co-sputtering of Cu, SnS and ZnS followed by annealing in N_2+20%H_2S gaseous environment at 580 °C for 3 hour. They have suggested preferential etching of metal oxides by socking of CZTS film in DI water to be beneficial for high performance [Hironori Katagiri et al., 2008]. Later in year 2011 Momose et al. has reported 3.7% PCE with CZTS absorber layer deposited using co-sputtering of Cu, Zn, Sn metals and annealing in sealed glass tube with elemental sulfur at 590 °C for 7 min [Momose et al., 2011]. Similar approach has been adopted by Htay et al. with stacked metallic precursors and has shown efficiency above 4% with cadmium free CZTS/ZnO heterostructure [Htay et al., 2011]. Scragg et al. has suggested that instability of back contact is the main culprit for the low efficiency of CZTS devices. They have deposited CZTS thin films using reactive pulsed DC magnetron co-sputtering followed by annealing at 560-570 °C for 10 min in different

environments. TiN intermediate layer has been employed in between CZTS and Mo for the passivation of back contact. An efficiency up to 7.2% has been achieved using this process, however the fabricated solar cells showed high series resistance suggesting a choice of more appropriate inert back contact material for intermediate layer is necessary for realizing higher efficiency [Scragg et al., 2013]. Tajima et al. used CZTS double layer deposition with high Cu concentration in CZTS near Mo back contact and lower Cu concentration in CZTS near the surface. Using this double layer architecture an improved Voc up to 0.78 V and the best CZTS solar cell efficiency of 8.8% is reported [Tajima, Itoh, Hazama, Ohishi, & Asahi, 2015].

2.5.2 Evaporation

Evaporation of constituent elements followed by annealing is an easy choice for the growth of CZTS thin films. The constituents can be evaporated either sequentially to form stacks or they can be evaporated simultaneously before annealing. Different evaporation techniques such as thermal evaporation, e-beam evaporation, coevaporation are employed for the deposition of CZTS thin films. Katagiri et al. for the first time introduced electron beam evaporation for depositing Cu/Sn/Zn stacked layers on soda lime glass (SLG) substrate, heated at 150 °C and later they annealed the evaporated stacks at 500 °C in N_2+5% H_2S gas environment to get kesterite CZTS thin film. A low conversion efficiency of 0.66% is recorded with Jsc ~ 6 mA/cm^2, Voc ~ 0.4 V and FF ~ 0.277 because of high resistivity (10 Ωcm) of the film [Hironori Katagiri et al., 1997]. Later they reported 2.62% [Hironori Katagiri et al., 2001] and 4.25% [H. Katagiri, Jimbo, Moriya, & Tsuchida, 2003] efficiency with ZnS/Sn/Cu stacking and suggested evaporation of sulfides to be beneficial rather than pure metal evaporation for better adhesion and surpassing the volume expansion during annealing. They also reported advantages of adding Na_2S layer before CZTS growth as is adopted in case of CIGS solar cell. Kobayashi et al. adopted the same stacking sequence and sulfurization temperature 520 °C for CZTS thin films and the maximum CZTS solar cell efficiency of 4.53% is achieved without any intentional doping such as Na [Kobayashi et al., 2005]. Akari et al. worked with different sequence of stacking in electron beam (EB) evaporation and suggested that Cu and Sn layer in the stacking should be adjacent for high performance CZTS device. They showed that Mo/Zn/Cu/Sn stacking perform relatively better with the maximum photoconversion efficiency 1.79% [Araki et al., 2008]. Thermal co-evaporation of Cu, Zn, Sn and S metal source is used by Wang et al. to fabricate CZTS solar cell with absorber layer thickness less than 1μm and showed efficiency up to 6.8%. They have performed detailed temperature dependent electrical characterization and suggested the presence of blocking back contact and dominant interface recombination are the main culprit for high series resistance and low open circuit voltage for CZTS solar cell [K. Wang et al., 2010]. Schubert et al. prepared kesterite phase CZTS with Cu rich composition using fast co-evaporation of ZnS, Cu, Sn and S. They showed the presence of binary CuS impurity phases in the prepared CZTS films. This impurity phase was removed by etching in KCN solution. An efficiency of 4.1 % has been reported using this technique [Schubert et al., 2011]. Shin et al. has reported the best PCE of 8.4% with CZTS device for very thin absorber layer (~600nm) [Shin et al., 2011]. In recent past Kato et al. has presented a record maximum efficiency of 9.2% obtained with pure sulfide CZTS solar cell. They have characterized front and back contact of the cell and suggest that ZnS segregation at the back contact may have beneficial effects such as back surface field for observed high efficiency [Takuya Kato, Homare Hiroi, Noriyuki Sakai, Satoshi Muraoka, 2012].

2.5.3 Electrodeposition

Electrodeposition is an attractive non vacuum technique for depositing CZTS thin film. Sequential layer deposition or single step co electrodeposition is used followed by annealing of deposited precursors in sulfur environment at an elevated temperature up to 600 °C for the growth of CZTS thin film on a conductive substrate. In 2008 Scragg et al. reported sequential deposition of Cu, Sn, and Zn layer on Mo-coated SLG substrate. Cu poor and Zn rich elemental composition with p-type conductivity is observed in CZTS film obtained after annealing precursor film in sulfur environment at 550 °C for 2 hours. However, they have not reported

any photovoltaic performance [Scragg, Dale, & Peter, 2008]. In 2009 Araki et al. tried sequential electrodeposition of Cu/Sn/Zn [Araki, Kubo, Mikaduki, et al., 2009] and co-electrodeposition of Cu, Zn, Sn precursor to prepare CZTS film [Araki, Kubo, Jimbo, et al., 2009] after annealing precursor film at 600 °C in sulfur environment. They have reported 0.98% and 3.16% PCE with sequentially electrodeposited and co electrodeposited CZTS film respectively. Ennaoui et al. has fabricated a 3.4% efficient CZTS solar cell and demonstrated the effect of light socking which improves the efficiency to 3.6% after 10 min of socking light before the measurements. They followed one step electrodeposition for elemental precursors followed by annealing at 550 °C in Ar + 5% H_2S gaseous environment [Ennaoui et al., 2009]. A 3.2% efficient kesterite CZTS solar cell is demonstrated by Scragg et al. adopting sequential electrodeposition with Cu/Sn/Cu/Zn stacking order and sulfurization at 575 °C for 2 hours in the sulfur environment [Scragg, Berg, & Dale, 2010].

2.5.4 Nanocrystal synthesis

Nano-crystal synthesis and associated deposition technique for CZTS are more promising, enabling phase formation prior to the film deposition and thus avoiding secondary phases. The controlled growth environment is provided for greater diffusivity of the constituent in the liquid phase to overcome activation energy barrier so as to allow the formation of thermodynamically stable phase. In other deposition techniques, CZTS phase formation occurs while annealing at elevated temperature, which results in the formation of several secondary phases and defects. In nanocrystal deposition the absorber film can be deposited directly at no or very low drying temperatures, thereby preserving the nano-crystalline properties of the film. Although this low-temperature film deposition gives flexibility of choosing substrates which can withstand low temperature, it allows extensive trapping of charge carriers because of the small size of nano-crystals which is not suitable for solar cells, degrading the performance. To overcome this issue, deposited nanocrystal films are heated at an elevated temperature in sulfur environment to enhance grain growth and reduce surface defects and grain boundaries. Guo et al. for the first time in 2009 reported a facile synthesis of CZTS nanocrystals with efficiency ~0.8% after selenization to form CZTS, Se absorber film [Q. Guo, Hillhouse, & Agrawal, 2009]. By further controlling the stoichiometry of the nanocrystalline film, they have reported 7.2% efficient CZTSSe solar cell [Q. Guo et al., 2010].

2.5.5 Sol-gel

Sol-gel deposition is one of the simplest deposition techniques involving direct liquid deposition of the constituents. CZTS sol-gel deposition primarily involves preparation of homogeneous precursor solution which is stable and has no precipitates. The prepared sol is used for spin coating and later annealed or dried at elevated temperature to form crystalline CZTS thin films. In 2007 Tanaka et al. for the first time prepared sol-gel precursor solution and prepared CZTS precursor films using spin coating the sol at 4000 rpm and drying films in air at 300 °C. The precursor film was later annealed at 500 °C in $N_2 + H_2S$ atmosphere for 1 hour to get CZTS film [K. Tanaka, Moritake, & Uchiki, 2007]. They showed 1.01% [K. Tanaka, Oonuki, Moritake, & Uchiki, 2009]and 1.61% [Moritake, Fukui, Oonuki, Tanaka, & Uchiki, 2009] efficient CZTS solar cell using all non-vacuum processed CZTS, suggesting the way to reduce the production cost of the solar cell. The observed low efficiency is due to the high resistivity of top Al: ZnO layer. Later they did a compositional dependent analysis of CZTS thin films and showed the highest conversion efficiency of 2.03% for Cu deficient CZTS film with Cu/(Zn+Sn) =0.8 [K. Tanaka, Fukui, Moritake, & Uchiki, 2011]. This is the highest efficiency to date reported with CZTS absorber prepared using the sol-gel technique.

2.6 Barriers towards high efficiency

Kesterite CZTS based solar cell has reached an efficiency of 9.2% with pure sulfide CZTS [Takuya Kato, Homare Hiroi, Noriyuki Sakai, Satoshi Muraoka, 2012], [Sun et al., 2016]and 12.7% with partial selenization in Se atmosphere [Jeehwan Kim et al., 2014]. However, these

reported efficiencies are far behind its theoretical limit and the high performing chalcopyrite counterpart [Green et al., 2018]. Identifying the bottlenecks is a deep concern governing the loss mechanisms responsible for the low efficiency of kesterite solar cells. The most severe loss in kesterite CZTS is observed due to the loss in fill factor and Voc of the device while the observed short-circuit current density has reached up to the level of the maximum Jsc reported with CIGS devices and thus not a serious concern for the kesterite cell efficiency [Siebentritt, 2013].

2.6.1 Narrow Phase stability

It is really difficult to obtain phase pure kesterite CZTS material because of its narrow region of phase stability and low thermal stability [Olekseyuk, Dudchak, & Piskach, 2004]. Apparently low thermal stability of CZTS at higher temperature is due to its ease of decomposition into volatile species such as S and SnS. Olekseyuk et al. investigated Cu_2S-ZnS-SnS_2 quasi-ternary system and showed the isothermal phase diagram for CZTS shown in **Figure 2.6**. It is shown that CZTS is stable only in a narrow region (region 1) of the phase diagram and any deviation from the stoichiometry results into the formation of undesirable secondary phases which are detrimental for the solar cell performance [Just et al., 2016].

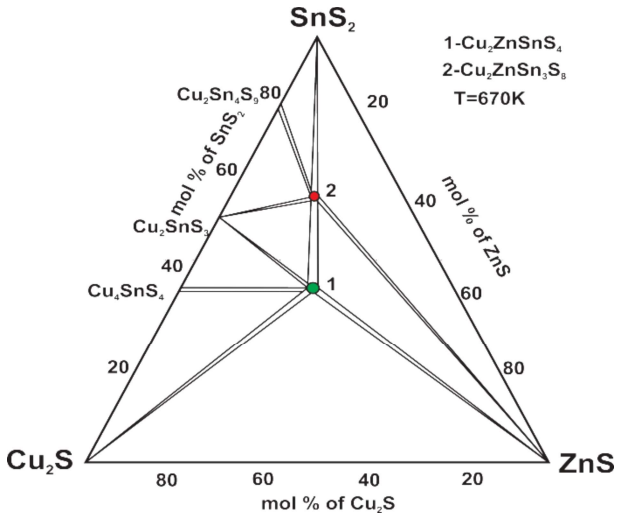

Figure 2.6 Phase diagram for CZTS taken from [Olekseyuk et al., 2004]

It is found that Cu and Sn-rich secondary phases segregate near the top of the absorber while zinc rich phases diffuse and accumulate near the back contact region during high-temperature annealing [Fairbrother et al., 2013]. High bandgap phases (e.g. ZnS) provides high series resistance to the device and can hinder the transport of charge carrier if present at the p-n junction. Further, presences of low bandgap phases (e.g. Cu_xS, SnS) at the junction deteriorate the open circuit voltage of the device by creating sub-bandgap energy levels at the absorber buffer layer interface. $Cu_{2-x}S$ being conductive (semi-metallic) in nature, its presence in CZTS provides shorting path between the front and back contacts [García, Nair, & Nair, 1999]. Presence of SnS_2 in CZTS can form secondary diode with the absorber because of its n type conductivity and can provide enhanced photo carrier recombination [Burton et al., 2013]. **Table 2.1** describes those possible secondary phases in kesterite with their band gap suggesting their detrimental impact on performance.

Table 2.1 Secondary phases in CZTS system with their bandgap, type of conductivity and their influence on the material properties

Phase	Bandgap (eV)	Type of Conductivity	Impact	Reference
Cu_2SnS_3	0.93-1.35	p	Create sub band gap level	[Berg et al., 2012]

Cu_2S	1.0-1.2	p	Shorting, Increases majority carrier concentration	
CuS	1.8-2.0	p	Shorting	
SnS_2	2.2-2.5	n	Low shunt resistance,	[Burton & Walsh, 2012]
Sn_2S_3	0.85	n	Form schottkey diode, increases series resistance	[Reddy & Kumar, 2016]
SnS	1.0-1.3	p	Decreases Voc	
ZnS	3.5-3.7	n	Increases Series resistance	

2.6.2 Defects in the absorber

Quaternary kesterite is prone to donor and acceptor intrinsic defects such as vacancies, antisites, and interstitials. Formation energy and a population of defects extremely depend on the stoichiometry of grown CZTS and change dramatically as the samples become nonstoichiometric. Defects with high formation energy are relatively insignificant and do not contribute in defining the electrical properties of the absorber. In CZTS formation energy of donor defects are quite high with respect to the acceptor defects and thus, making the system intrinsic p-type characteristics without any intentional doping [S. Chen, Yang, Gong, Walsh, & Wei, 2010]. A representative acceptor and donor defect levels in the CZTS is shown in **Figure 2.7**.

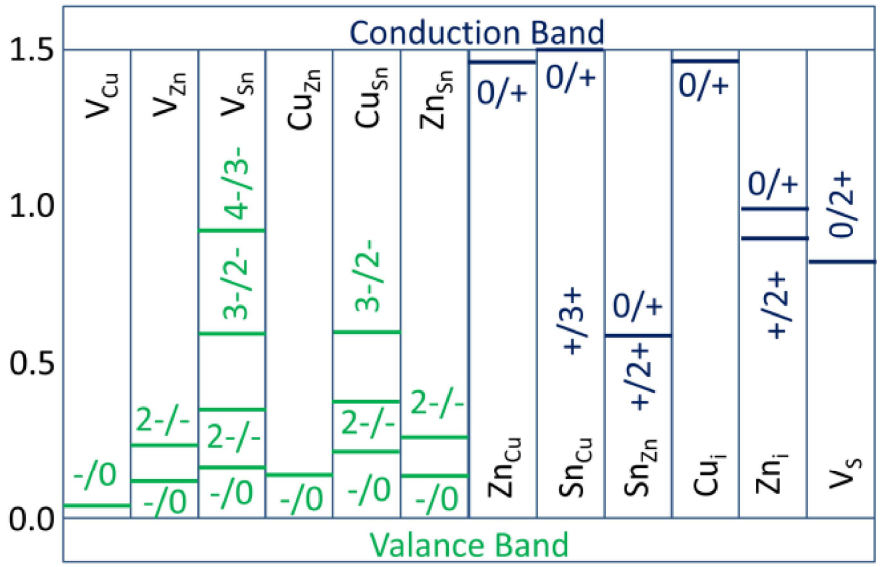

Figure 2.7 Representative defect levels in CZTS taken from reference [S. Chen, Walsh, Gong, & Wei, 2013]

Copper vacancy V_{Cu} and antisite Cu_{Zn} i.e. copper at zinc site are two dominant shallow acceptor defects in CZTS with Cu_{Zn} level deeper with respect to V_{Cu}, **Figure 2.7**. All other accepter defects are less populated because of their high formation energies and hence not much significant for CZTS device. Among donor defects, Zn_{Cu} has shallower defect level and is relatively non-influential because of the nearly identical atomic structure of Cu and Zn. In CZTS single donor level due to Sn_{Cu} (0/+) is extremely shallow while double donor Sn_{Cu}(+/3+) is deep in the bandgap. Due to multivalent nature of Sn, it can exist at both Cu and Zn site. For Cu poor and Sn rich stoichiometry, the formation energy of Sn_{Cu} and Sn_{Zn} antisite defects decreases and can have a high population, and thus, may hamper the device performance. Defect level introduced

due to sulfur vacancy is deep in the band gap and has formation energy quite low for CZTS with a high cation to anion ratio. This suggests the need for sufficient sulfurization for improved CZTS solar cell performance. The presence of both donor and acceptor defects in CZTS allow formation of multitude of self-compensating defect cluster such as [Cu_{Zn} + Zn_{Cu}], [Zn_{Sn} + Sn_{Zn}], [V_{Cu} + Zn_{Cu}] etc. Among all defect cluster [$2Cu_{Zn}$ + Sn_{Zn}], [V_{Cu} + Zn_{Cu}] and [Zn_{Sn} + $2Zn_{Cu}$] clusters have comparatively lower formation energy and contribute significantly in non-stoichiometric CZTS. For Zn rich and Cu poor stoichiometry, population of [V_{Cu} + Zn_{Cu}] and [Zn_{Sn} + $2Zn_{Cu}$] clusters is high while [$2Cu_{Zn}$ + Sn_{Zn}] cluster shows high population in Cu rich and Sn rich samples [S. Chen et al., 2013]. Presence of defects and defect clusters in CZTS creates recombination centers within the bandgap and results in large open circuit voltage loss.

2.6.3 Band offset at hetero interface

The band alignment at the heterojunction interface is governed by the electron affinity values of the materials forming the heterojunction. Electron affinity is basically a material specific property and is equal to the energy required for an electron to move it from the conduction band to the vacuum level as represented schematically in **Figure 2.8**. The band alignment at the heterointerface depends on the electron affinity difference between the heterostructure materials forming the junction. Based on the electron affinity differences, the band alignment at the heterojunction can be classified into three broad categories: straddling (type I), staggered (type II) and broken gap (type III) as shown in **Figure 2.9**. In type I heterostructure energy bandgap of one material is completely lies within the bandgap of second material, **Figure 2.8 & 2.9**. In type II heterostructure bandgap of one material partially overlap the bandgap of second material, **Figure 2.9**. In type III heterostructure there is no overlap between the bandgap of two materials, **Figure 2.9**.

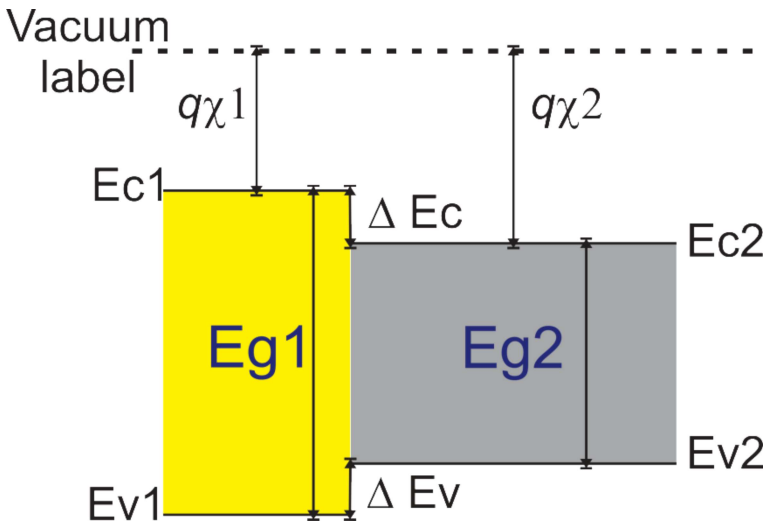

Figure 2.8 Schematic representation of valence and conduction band offset at hetero interface

The conduction band offset at the heterointerface is defined as the difference in the electron affinity value of the materials forming the heterostructure, **Figure 2.8**.

$$\Delta E_c = q(\chi_2 - \chi_1)$$

Further, the valence band offset can be written as

$$\Delta E_v = (E_{g1} - E_{g2}) - \Delta E_c$$

or,

$$\Delta E_v = \Delta E_g - \Delta E_c$$

The band alignment at the hetero-interface dramatically affects the solar photovoltaic performance. The limited solar photovoltaic performance of kesterite is mainly attributed to the large open circuit voltage deficit. The reason behind this voltage deficit is the non-optimum

conduction band alignment of the heterostructure between the absorber layer and the buffer layer.
A large cliff resulting from type II band alignment at the hetero-interface lowers the open circuit voltage while spike at the heterostructure interface due to type I band alignment reduces the short circuit current density (Jsc) of the device. These cliff and spike like band alignment affect carrier dynamics across the heterointerfaces. For example, trap assisted recombination is dominant in case of type II heterostructure while spike at the heterointerface offers large barrier to the photo generated charge carries resulting in the reduced short circuit current density of the device. It is necessary to optimize the band offset at the heterojunction interface as both the situations hinder the efficiency of solar cell.

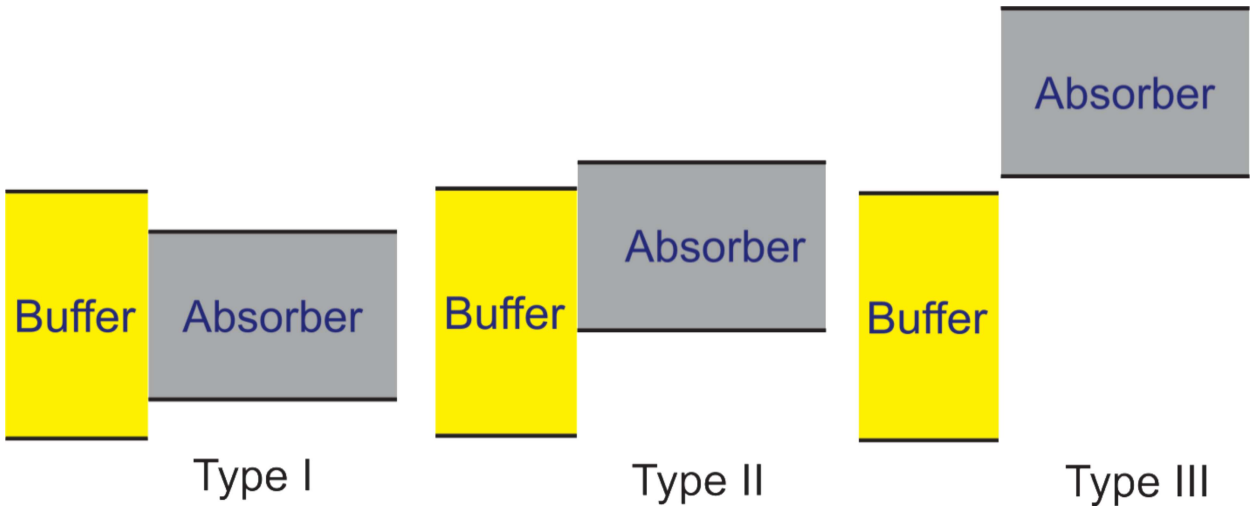

Figure 2.9 Schematic representation of type of band alignment at the heterointerface

CdS is a commonly used buffer layer with CZTS solar cell and is well adopted from CIGS solar cell architecture. The choice of a suitable buffer layer material is needed for further enhancement in CZTS solar cell performance. Type I and Type II heterostructure are considered suitable for high open circuit voltage and high short circuit current, respectively. Thus, a tradeoff between CZTS absorber and buffer layer is desired for optimal open circuit voltage and short circuit current. Different buffer layer materials have been investigated for heterostructure combination with CZT(S,Se) absorber layer. The observed band offset in the conduction and valence band is shown in **Table 2.2** in conjunction with type of band offset.

Table 2.2 Conduction band offset (CBO), Valance band offset (VBO) and the type of heterostructure interface for different buffer layer combination with CZTS,Se heterostructure.

Buffer layer material	*Interface*	*CBO*	*VBO*	*Type*	*Reference*
CdS	CZTS	-0.24±0.10 eV (XPS) -0.18±0.10 eV (NEXAFS)	-1.14±0.10 eV	II, Cliff	[Yan et al., 2014]
	CZTS	0.41 eV (UPS)	-0.54±0.07 eV	I, Spike	[Haight et al., 2011]
	CZTSe	0.48 eV (UPS)	-0.97±0.07 eV	I, Spike	[Haight et al., 2011]
	CZTS	-0.06 eV	-0.96 eV	II, cliff	[J. Li et al., 2012]
	CZTS	-0.33±0.15 eV	-1.2 ±0.15 eV	II,cliff	[Bär et al., 2011]
	CZTS	-0.34±0.06 eV	-1.2 4±0.06 eV	II,cliff	[Santoni et al., 2013]

	CZTS	-0.1±0.1 eV	-1.1±0.1 eV	II,cliff	[Kataoka et al., 2016]
Zn(O,S)	CZTS	0.92±0.10 eV (XPS) 0.87±0.10 eV (NEXAFS)	-0.98±0.10 eV	I, Spike	[Yan et al., 2014]
ZnS	CZSSe	1.1 eV	-1.3 eV	I, Spike	[Barkhouse et al., 2012]
ZnO	CZTSSe	±0.1 eV	-2.1 eV		[Barkhouse et al., 2012]
$Zn_xSn_{1-x}O_y$	CZTS	+0.1		I, spike	
$Zn_{1-x}Cd_xS$	CZTS	0.37 eV	-0.83 eV	I, Spike	[Sun et al., 2016]
In_2S_3	CZTS	0.41±0.10 eV (XPS)	-0.19±0.10eV	Spike	[Yan et al., 2014]
	CZTS	0.11eV	-0.73 eV	I, spike	[Jiang et al., 2016]
	CZTSSe	0.15±0.1 eV	-0.75eV	spike	[Barkhouse et al., 2012]
CeO_2	CZTS	-0.12±0.2 eV	-1.92±0.14 eV	II, cliff	[Crovetto et al., 2016]

2.6.4 Non-optimum back contact

Considering the advantages associated with molybdenum used as a back contact material in CIGS solar cell, it is simply replicated in CZTS based solar cell. During the growth of CIGS, Se over Mo, a thin layer of $Mo(S/Se)_2$ is formed. This provides good adhesion to the substrate and acts as a diffusion barrier to the impurities from commonly used SLG substrate. It helps in forming ohmic back contact with CIG(S, Se). However, the effectiveness of Mo with CZTS is still not very clear. $Mo(S/Se)_2$ is usually formed during the high-temperature annealing of CZTS/Se with chalcogen diffusion from the bulk absorber to Mo back contact [Shin, Bojarczuk, & Guha, 2013]. It is reported that a thin layer of MoS_2 less than hundreds of nanometer is beneficial with the cell architecture while it's higher thickness acts adversely and causes increased series resistance and thereby reduces the cell efficiency [Juran Kim et al., 2016].

2.7 Possible improvements for efficiency boost

The performance of CZTS, Se solar cell is still far below the theoretically expected efficiency. The prime barrier in the efficiency boost is mostly due to the difficulties in reducing the open circuit voltage deficit. The p-n heterostructure interface between buffer and CZTS layer and interface at the back contact are the main source of this voltage deficit. Unavoidable presence of secondary phases in the bulk and at the interface of absorber layer also lower fill factor of the device by introducing parasitic resistances. A number of possible methods can be tried to improve the device performance which are discussed in the following sections.

2.7.1 Preferential etching of absorber

Among all other factors causing poor performance of CZTS based solar cells, simultaneous growth of secondary and ternary phases are major drawback associated with this system. The narrow thermodynamic phase stability of CZTS due to volatile constituents (S, Sn), allows the coexistence of impurity phases in conjunction with CZTS kesterite phase. The precise control of the elemental composition is very difficult for CZTS system. Further, the need of non-stoichiometry for high efficiency also leads to the simultaneous growth of unwanted secondary phases. To get rid of these impurity phases, a preferential etching of absorber is proposed to avoid any efficiency loss. Etchant also improves the surface of CZTS and thus assists in making

a less defective heterointerface with an n-CdS layer, thereby reducing the recombination centers at the interface. KCN serves as a better etchant for Cu rich impurity phases and does not dissolve ZnS and SnS. Removal of Cu rich phases from the surface improves open circuit voltage and fill factor of the device, thus improves the overall device performance [T. Tanaka et al., 2012]. NH_4OH etches CuS and partially ZnS phases without disturbing Sn phases [Erkan, Chawla, Repins, & Scarpulla, 2015][Timmo et al., 2010]. Concentrated HCl can remove tin chalcogenides [Redinger et al., 2014]. 10% v/v of HCl removes ZnS completely with partial etching of SnS while CuS remains insoluble in HCl [Fairbrother et al., 2012]. Different oxidizing agents such as hydrogen peroxide (H_2O_2), potassium dichromate ($K_2Cr_2O_7$), permonosulfuric acid (H_2SO_5), persulfate (Na_2SO_5, $Na_2S_2O_8$) etc. can easily oxidize unwanted sulfides from CZTS [Chavda, Patel, Mukhopadhyay, & Ray, 2016]. The following **Table 2.3** reviews different etchants useful for preferential etching of different secondary phases.

Table 2.3 Compound to be etched with etchant solution, concentration and time required for etching

Compound	*Etchant*	*Concentration*	*Time*	*Observation*	*Reference*
$Cu_{2-x}S_y$	KCN	10 w%	1 min	Cu_xS_y from Cu rich CZTS	[Bär et al., 2011][Mousel et al., 2014]
$Cu_{2-x}(S,Se)$	2-mercaptoethanol + ethylenediamine	1:4 ratio by volume	20 min	$Cu_{2-x}(S,Se)_y$ from Cu rich CZTS	[Pinto, Shin, Aydil, & Penn, 2016]
Cu_xS	H_2O_2	6% H_2O_2, PH=9.0	1-2 min	Cu based secondary phases	[Chavda et al., 2016]
CuS, Na, O_2	NH_4OH+DI water	62.5ml 14.8M NH_4OH +366 ml DI water	1 min	Surface oxides, CuS and partially Zn	[Erkan et al., 2015][Timmo et al., 2010]
SnSe	HCl	37 vol%	10 min	ZnS, Sn and chalcogen	[Redinger et al., 2014]
ZnS, SnS	HCl	10% v/v at 75° C	10 min	Completely etches ZnS and partially etches SnS	[Fairbrother et al., 2012]
Zn(S,Se)	$KMnO_4/H_2SO_4$ +Na_2S	0.01M $KMnO_4$/1M H_2SO_4	1 min	Removes Zn(S,Se) phase	[Lõpez-Marino et al., 2013]
Cu_2SnSe_3	Br_2-MeOH	0.02M Br_2+methanol	1 min	Removes Cu and Sn based ternary chacogenide	[Mousel et al., 2013]
Sn(S,Se)	$(NH_4)_2S$	22%w/w	1 min	Selective removal of Sn(S,Se), Cu and Zn phases insoluble	[Xie et al., 2014]

2.7.2 Intermediate layer between absorber and back contact

Back contact material for CZTS is not yet fully optimized and well understood. Mo is the most widely used back contact material in CZTS solar cell but its effectiveness is still not completely understood. The high temperature is essential to get phase pure CZTS. This allows diffusion of sulfur from CZTS towards Mo back contact and forms a thin layer of MoS_2. The thickness of MoS_2 layer depends on the annealing temperature and duration. A small thickness of MoS_2 is considered beneficial as it helps in forming ohmic contact with CZTS. However, if the

thickness of MoS_2 is large, it shows reverse diode characteristics at the back contact and thus decreases the current collection efficiency. Dhakal et al. showed the formation of Schottky junction at Mo/MoS_2 interface and suggested that MoS_2 is not a barrier to the hole transport at the back contact [Dhakal, Harvey, Van Hest, & Teeter, 2015]. However, with lowering thickness of MoS_2 layer growth, several advantages have been observed such as reduction in series resistance of the device. To restrict the formation of MoS_2 at the back contact surface a thin intermediate layer is grown on the top of Mo layer before deposition of CZTS absorber. Several such intermediate layers have been tried so far to improve the efficiency of CZTS solar cell and are summarized in **Table 2.4**. Implementing intermediate layer offers advantages by reducing the diffusion of sulfur from CZTS towards Mo and thus reduces the growth of MoS_2 layer. Presence of intermediate layer also restricts the formation of voids and secondary phases such as ZnS and SnS_2 at the back contact [Cui et al., 2015]. However, some negative impacts such as inferior crystal quality, increased series resistance of the device are also reported for such intermediate layers [F. Liu et al., 2014].

Table 2.4 Intermediate layer with their thickness and impact on device parameters

Intermediate layer	*Absorber*	*Thickness (nm)*	*Voc (mV)*	*Jsc (mA/cm^2)*	*FF (%)*	*Efficiency (%)*	*Rs (Ωcm^2)*	*Rsh (Ωcm^2)*	*Observation*	*References*
TiN	CZTSe	20	264/385	25.4/42.6	44/54.2	2.95/8.9	3.4/1.8		Inhibit formation of MoSe2	[Shin, Zhu, Bojarczuk, Jay Chey, & Guha, 2012a]
TiN	CZTS	10-20	667/621	19.6/18.7	60/47.1	7.9/5.5	2/6.9		Passivate Mo surface, Increases series resistance	[Scragg et al., 2013]
ZnO	CZTS	10	609/635	17.19/17.84	58.8/58.9	6.45/6.68	4.87/4.74	7.39/8.02	Prevent Zn diffusion into MoS2	[R. Liu et al., 2016]
ZnO	CZTSe	10	314/364	19.7/28.6	40.2/57.5	2.5/6	3.7/<0.1	44/149	Reduction in voids, reduced series resistance	[Lopez-Marino et al., 2013]
ZnO	CZTS	10	324/641	10.8/15.97	32/42	1.13/4.3	19.7/15.1	152/1630	Reduces formation of voids, SnS2, and MoS2, Improved series and shunt	[X. Liu et al., 2014]

									resistance	
Ag	CZTS	20	476/597	11.92/15.05	40.7/49.2	2.31/4.42	19.5/12.8		Inhibit formation of voids ,SnS_2, MoS_2	[Cui et al., 2016]
Ag	CZTS	20	360/596	11.64/14.38	33.8/41	1.42/3.51		48/180	Reduction in MoS_2,ZnS,SnS_{2-x}, Compensate carrier concentration of CZTS	[Cui et al., 2015]
TiB_2	CZTS	30	658/598	9.56/13.21	49/56	3.06/4.4	22/10.3		Inhibit formation of MoS_2, degrades crystal quality of absorber	[F. Liu et al., 2014]
C	CZTS	25	560/560	13.6/16.96	55/56	4.47/5.52	5.1/2.0		Carbon aggregates in voids and provides a better connection between CZTS and MoS_2/Mo	[Zhou et al., 2015]
C	CZTS,Se	26	399/439	26.8/27.9	57.8/59.16	6.2/7.24	1.78/0.53		Reduces voids and $MoSSe_2$ thickness, improves crystallinity, reduces series resistance	[Zeng et al., 2015]
Bi	CZTS	20	555/590	12.5/15.7	51/51	3.59/4.75	6.43/5.67		Improves crystallinity, reduces MoS_2 formation, decreases series resistance	[Tong et al., 2016]
MoO_x	CZTS	10	541/620	17.2/18.1	57.2/57.3	5.32/6.52	3.6/3.0	194/392	Allow enhanced Na diffusion, Improves crystallinity	[Park et al., 2018]

2.7.3 Alkali metal doping

In CIGS solar cell grain growth is widely influenced by the presence of alkali metals mainly Na. Presence of Na in the absorber allows enhanced grain growth and passivates grain boundary defects that finally leads to the enhanced solar cell efficiency [Kronik, Cahen, & Schock, 1998][Wei, Zhang, & Zunger, 1999]. Nagaoka et al. observed that sodium doping in CZTS enhances the majority carrier hole concentration in CZTS single crystal. They showed experimentally that incorporation of Na at the cation antisites increases p-type carrier concentration and hole mobility of the absorber. The introduction of Na decreases the activation energy of thermally activated carrier and increases the open circuit voltage of the device thus enhancing the cell efficiency [Nagaoka et al., 2014]. Johnson et al. experimentally showed the impact of Na, K, Ca, Al and Mg atoms which are common constituents of soda lime glass and suggested that diffusion of Na and K only affects the film morphology and electrical properties. They suggested that alkali metal segregates at the grain boundary and acts as a fluxing agent and locally lowers the melting point. This local lowering in melting point, in turn, increases the mobility of cations and speed up the grain growth [Johnson et al., 2014]. Introduction of Na in CZTS is quite easier as Na diffuses through Mo at high temperature and facilitates large grain growth. Potassium is even more favorable for the grain growth but it requires an additional source of K to be present during the high-temperature annealing step of CZTS.

2.7.4 Implementing double layer architecture

Open circuit voltage deficit in kesterite CZTS solar cell is a major hurdle to achieve the high efficiency. Increasing carrier concentration helps to improve the open circuit voltage. However, it also increases the minority carrier life time. To counter these compensating behavior, a double layer absorber structure is implemented by Tajima et al [Tajima et al., 2015]. Highly doped CZTS absorber layer at the back contact and shallowly doped bulk at the interface with the n-type CdS buffer layer is formed to realize p-i-n structure [Tajima et al., 2015]. This improved structure increases the inner potential between CZTS and the buffer layer and an improved open circuit voltage of 0.78 V is realized. Double layer absorber structure also reduces the possibility of forming shunt path between the top and bottom electrode thus improving the fill factor of the device [Yan et al., 2017].

2.7.5 Substitution with foreign elements

Partial substitution at the native sites of CZTS can be helpful in realizing the improved inefficiency. Insertion of Se atom in place of S allows lowering the band gap of the material. The high performing CZTS based solar cells are alloyed partially with Se atom. Theoretical calculations suggest that the formation energy of donor defects such as Sn_{Zn} and $V_{S/Se}$ in CZTSe is relatively high as compared to that of CZTS. Further, with an increase in (S/(S + Se)) ratio shifts valance band maxima to the lower energy resulting in deeper defect levels in the band gap. These deep defects and high defect densities exhibit severe band tailing problem in the sulfur-rich compound. This band tailing problem is more severe in CZTS as compared to CZTSe and is detrimental causing a higher loss of open circuit voltage. It is suggested that CZTSe shows spikes at the conduction band offset while CZTS shows cliff type conduction band offset at the heterointerfaces with CdS buffer layer. It is seen that solar cell with lower (S/(S + Se)) ratio shows better performance possibly due to the better band alignment and reduced deep level traps. CZTS also provides high series resistance due to the formation of wide band gap ZnS as compared to ZnSe which is formed in CZTSe. Hence, it is favorable to have small (S/(S + Se)) ratio in CZTS, Se device.

Synthesis of phase pure CZTS is a bit difficult and challenging due to its narrow region of phase stability. The volatility of Sn causes difficulties in controlling the phase and stoichiometry of CZTS. Substitution of Sn in CZTS from other group IV elements such as Ge and Si can tailor further the electrooptic properties of CZTS material. Substitution of Ge in place of Sn can tailor the bandgap from 1.5 eV to 2.1 eV while Si substitution can change the bandgap up

to 2.7 eV [Vishwakarma, Varandani, Shivaprasad, & Mehta, 2018]. This wide range tunability of bandgap can also help in selecting a wide bandgap material for their application in tandem solar cell structure. Moreover, substitution of Sn also helps in avoiding the multivalent defects such as Sn_{Cu} due to the multivalent +II and +IV oxidation states of Sn.

2.8 Experimental characterization

In this section, we discuss different characterization techniques used for structural, microstructural, optical and electronic properties of prepared thin films.

2.8.1 X-ray diffraction (XRD) technique

X-ray diffraction technique is a powerful and non-destructive tool to analyze the structural properties of materials such as structure, phase, and crystallite size. X-ray was first discovered by a German Physicist 'Wilhelm Conrad Rontgen' in 1885 which is an electromagnetic radiation lies in the wavelength range 0.01- 100 Å. In 1912 Max von Laue had first discovered that a crystalline material behaves like a three dimensional grating for X-rays. X-ray diffractometer has three basic units, an X-ray tube, a sample holder and an X-ray detector. X rays are generated by bombarding thermally generated high energy electrons on a target under vacuum in cathode tube, which knock out inner cell electrons of the target material, thus generating characteristic X-rays of the target material. The generated X-ray is then passed through the Soller slit and a collimated X-ray beam is formed. This collimated X-ray beam is passed through a divergence slit and made to fall on the sample mounted on the sample holder. The diffracted beams from the sample are then collected at the detector.
We have used D8 Advance Powder X-ray diffractometer with a characteristic Cu-kα wavelength of 1.54 Å as incident X-ray radiation. The details of the parameters used during the measurement are explained in subsequent chapters.

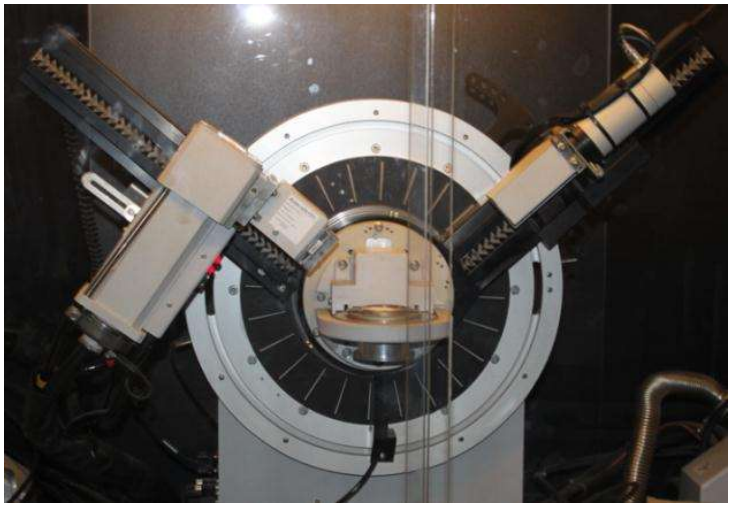

Figure 2.10 Camera image of X-ray diffractometer at IIT Jodhpur

2.8.2 Scanning electron microscopy (SEM)

Scanning electron microscopy is used to analyze the surface and microstructure, using a focused beam of high energy electrons that interact with the materials' surface and generates different signals. The generated signals, after material-electron interaction, include secondary electrons (used for imaging), backscattered electrons (used for imaging and determining the orientation of material), characteristics X-rays (used to determine elemental composition) etc. Secondary electrons are mostly used to see the surface morphology and the topography of the sample while back scattered electrons are mostly used for contrast imaging to distinguish different phases in the multiphase system. X-rays generated due to the material and electron interaction is used to find out the elemental composition present in the material. Carl Zeiss SEM

EVO 18 special edition has been used for cross-sectional and surface imaging of the prepared samples.

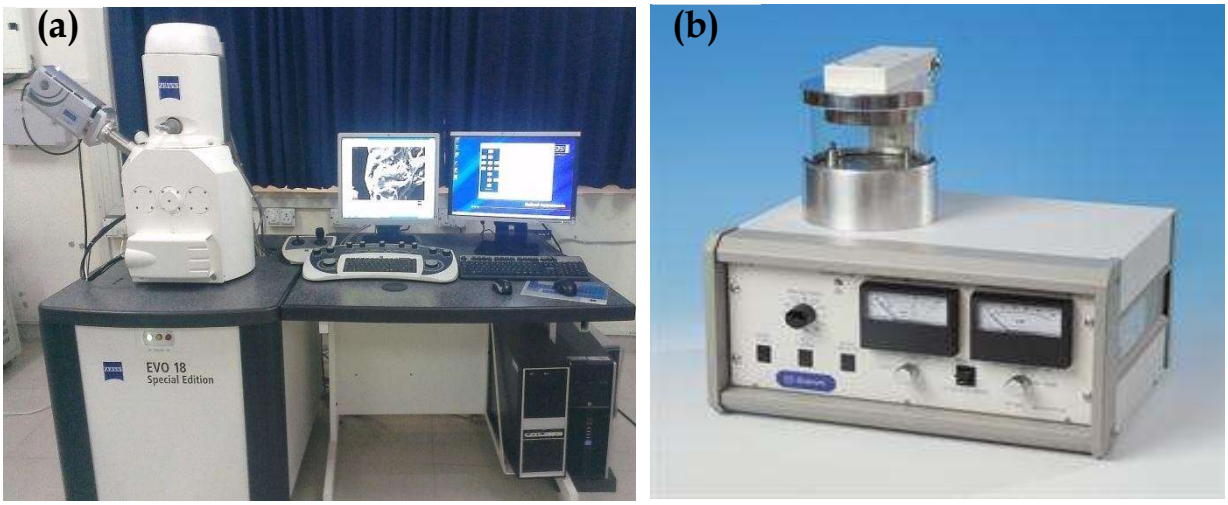

Figure 2.11 Camera image of (a) Scanning electron microscope and (b) DC sputter coating unit at IIT Jodhpur

2.8.3 Energy dispersive X-ray spectroscopy (EDS)

Electron-material interaction generates various signals including X-rays. In energy dispersive X-ray spectroscopy (EDS) technique an EDS detector is used which separates X-ray generated from different elements present in the material into energy spectrum. This is analyzed to determine the elemental composition present in the specimen. Oxford make (X-act) EDS detector is attached with Carl Zeiss SEM EVO 18 special edition is used to determine the elemental composition of the materials used in this thesis.

2.8.4 Atomic force microscope (AFM)

Atomic force microscope comprises of an atomically sharp tip which scans over a surface and through feedback mechanism piezoelectric scanners are maintained to keep the force or height of the tip constant above the sample surface. In constant force mode, deviation in the height of the tip and in constant height mode, the deflection force on the sample is recorded to see the three-dimensional topographic image of the surface.
Park system scanning probe microscopy (SPM), XE-70 system is used to find out the topographic images, roughness, probable surface defects, and average grain size of the samples. Further details are discussed in the chapters wherever AFM results are presented.

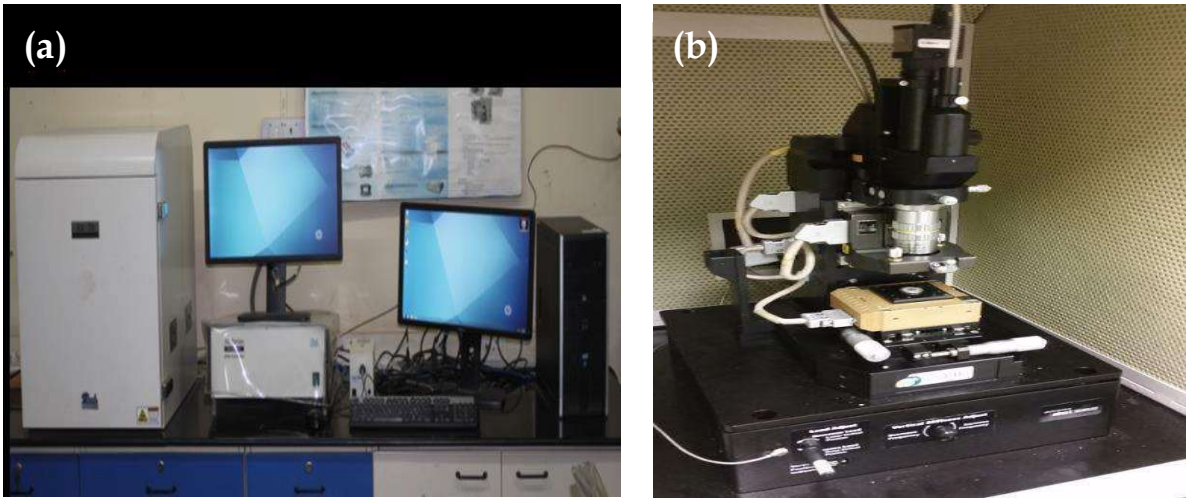

Figure 2.12 Camera image of Atomic force microscope (AFM) system at IIT Jodhpur

2.8.5 UV-Vis spectrophotometer

Agilent Cary 4000 UV-Vis spectrophotometer is used to analyze the optical properties of the material. Optical transmittance and absorbance of the material are taken keeping substrates as the reference and material coated over the substrate as the sample. To obtain diffuse reflectance spectra diffuse reflectance accessories are equipped (DRA) with the system which allows collecting diffuse and/or diffuse plus specular reflectance. An integrating sphere coated with polytetrafluoroethylene (PTFE) is used in the DRA with a respective spectral detector which can collect and measure electromagnetic radiation. PTFE is a white diffusive material with reflectivity above 99% in 300 to 1800 nm wavelength range. In diffuse reflectance measurement, PTFE is taken as a reference and the diffused reflectance from the sample mounted on the reflectance port is collected by the integrating sphere.

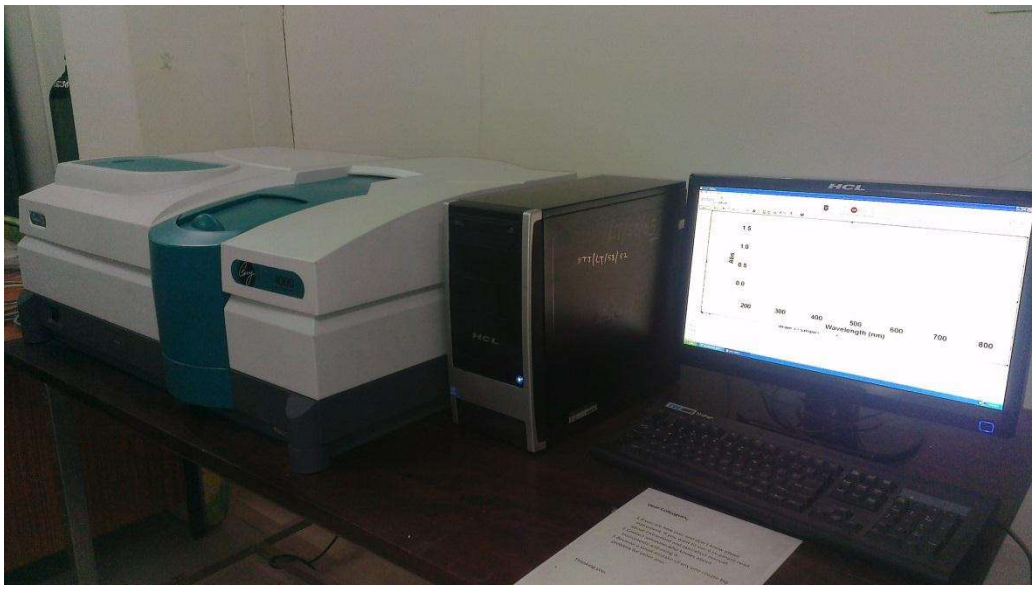

Figure 2.13 Camera image of Cary 4000 UV- Vis spectrophotometer

2.8.6 Infrared and Raman spectroscopy

Bruker FTIR vertex 70v spectrometer is used to measure the vibrational spectra due to change in molecular dipole moment in the samples. Reflectance spectra are measured by taking gold reflectance as a reference. In transmittance measurement, pure potassium Bromide (KBr) pallet is taken as a reference sample. A sample (mostly powder samples) is mixed with KBr and a homogeneous transparent thin pellet of this mixture is formed to collect the spectra in the range 2.5 to 25 μm wavelength.

Raman spectroscopy analyzes the inelastic scattering of light that is generated after the interaction of monochromatic radiation with the lattice vibrations in molecules and crystals. NomadicTM Raman Microscope (Bay Spec, USA make) equipped with multiple excitation sources (355 nm, 532 nm, and 785 nm), is used for Raman vibrational spectroscopy measurements. The system also consists of dedicated optimized detectors for individual wavelength source to ensure optical spectral coverage, resolution, and sensitivity. It is also featured with integrated laser control and motorized ND filters for adjusting laser power. Olympus optical microscope integrated with the motorized stage is provided for transmittance and reflectance mode operation. A charged coupled device (CCD) camera is equipped on the top of the microscope for capturing bright field image. Further details about the experiment are discussed in the subsequent chapters.

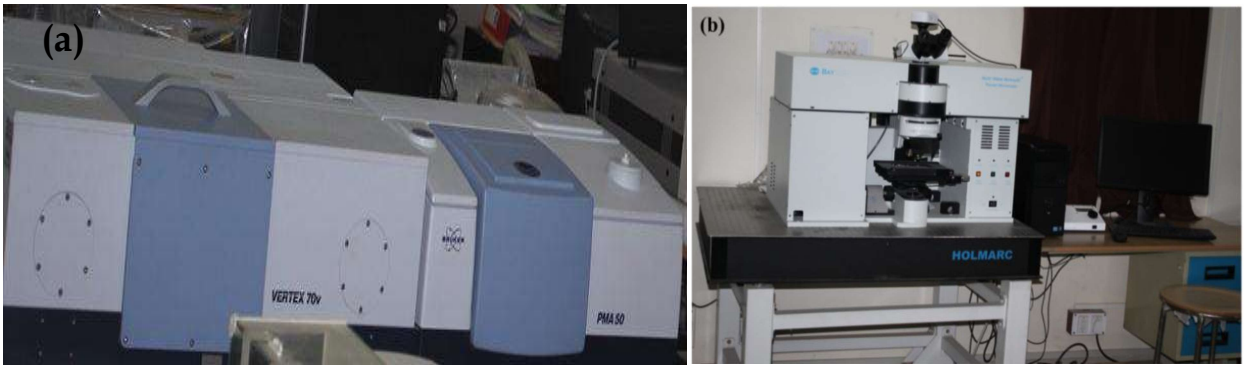

Figure 2.14 Camera image of (a) Fourier transform infrared spectrometer and (b) Raman spectrometer unit at IIT Jodhpur

2.8.7 Electrical and impedance characterization

Keithley 4200 semiconductor characterization system (SCS), **Figure 2.15 (a)**, is used to measure current-voltage (*I*–*V*) and resistivity characteristics of the samples in two and four probe geometries, respectively. Electrical characterization of the solar cell is done under dark and under one sun (100 mW/cm^2) illumination. The illumination is maintained by a Xenon lamp and the light intensity at the sample is calibrated using flux meter by varying the distance between the sample surface and illumination source. Electrochemical and impedance characteristics are measured using Autolab PGSTAT302N (Matrohm make) electrochemical workstation, **Figure 2.15 (b)**, equipped with a frequency analyzer unit.

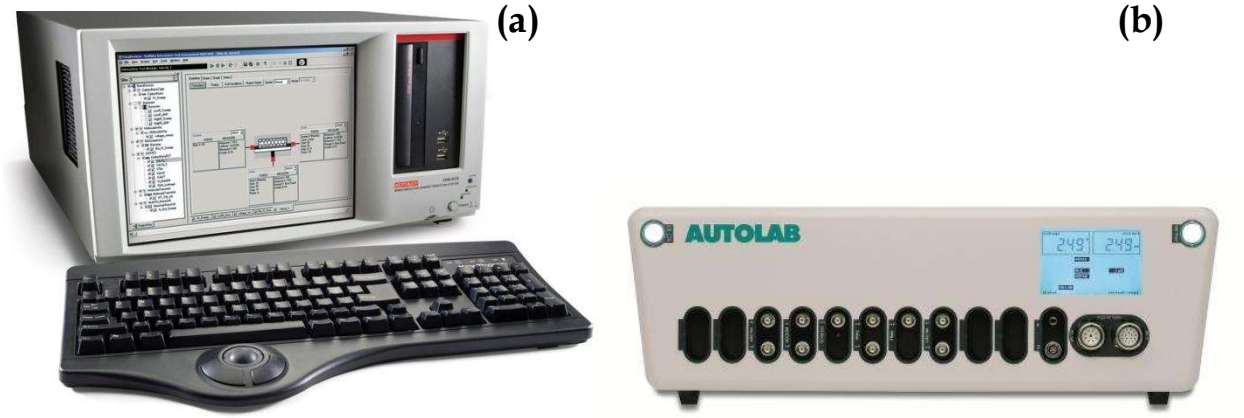

Figure 2.15 Camera image of (a) Semiconductor characterization system (SCS) and (b) Electrochemical workstation at IIT Jodhpur